CHEMISTRY OF MATERIALS

Article

pubs.acs.org/cm

Dual Substitution Strategy to Enhance Li^+ Ionic Conductivity in $Li_7La_3Zr_2O_{12}$ Solid Electrolyte

Lucienne Buannic,*[,†] Brahim Orayech,[†] Juan-Miguel López Del Amo,[†] Javier Carrasco,[†] Nebil A. Katcho,[†] Frédéric Aguesse,[†] William Manalastas,[†] Wei Zhang,[†,‡] John Kilner,[†,§] and Anna Llordés*[,†,‡]

[†]CIC EnergiGUNE, Parque Tecnológico de Álava, 48, 01510 Miñano, Álava, Spain

[‡]IKERBASQUE, The Basque Foundation for Science, 48013 Bilbao, Spain

[§]Department of Materials, Imperial College, London SW7 2AZ, United Kingdom

Supporting Information

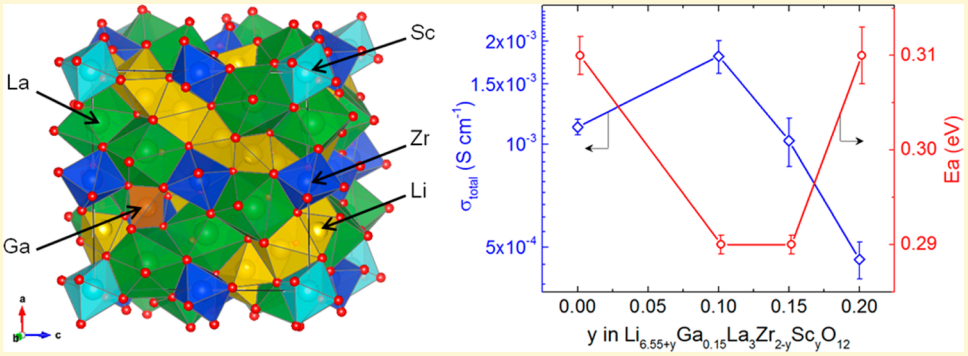

ABSTRACT: Solid state electrolytes could address the current safety concerns of lithium-ion batteries as well as provide higher electrochemical stability and energy density. Among solid electrolyte contenders, garnet-structured $Li_7La_3Zr_2O_{12}$ appears as a particularly promising material owing to its wide electrochemical stability window; however, its ionic conductivity remains an order of magnitude below that of ubiquitous liquid electrolytes. Here, we present an innovative dual substitution strategy developed to enhance Li-ion mobility in garnet-structured solid electrolytes. A first dopant cation, Ga^{3+}, is introduced on the Li sites to stabilize the fast-conducting cubic phase. Simultaneously, a second cation, Sc^{3+}, is used to partially populate the Zr sites, which consequently increases the concentration of Li ions by charge compensation. This aliovalent dual substitution strategy allows fine-tuning of the number of charge carriers in the cubic $Li_7La_3Zr_2O_{12}$ according to the resulting stoichiometry, $Li_{7-3x+y}Ga_xLa_3Zr_{2-y}Sc_yO_{12}$. The coexistence of Ga and Sc cations in the garnet structure is confirmed by a set of simulation and experimental techniques: DFT calculations, XRD, ICP, SEM, STEM, EDS, solid state NMR, and EIS. This thorough characterization highlights a particular cationic distribution in $Li_{6.65}Ga_{0.15}La_3Zr_{1.90}Sc_{0.10}O_{12}$, with preferential Ga^{3+} occupation of tetrahedral Li_{24d} sites over the distorted octahedral Li_{96h} sites. ^{7}Li NMR reveals a heterogeneous distribution of Li charge carriers with distinct mobilities. This unique Li local structure has a beneficial effect on the transport properties of the garnet, enhancing the ionic conductivity and lowering the activation energy, with values of 1.8×10^{-3} S cm^{-1} at 300 K and 0.29 eV in the temperature range of 180 to 340 K, respectively.

INTRODUCTION

Safety issues related to Li-ion batteries have become of general concern and are currently limiting their further development for powering larger scale devices such as electric vehicles or aircraft.[1−3] The replacement of flammable and toxic organic liquid electrolytes with inorganic solid electrolytes will offer a tremendous increase in safety, preventing thermal runaway in case of battery failure.[4] Additionally, it will also boost the energy density of the cell as inorganic electrolytes can be combined with both high voltage cathodes—unlike liquid electrolytes[5]—and with Li metal anodes. Among the most suitable inorganic solid electrolyte candidates, $Li_7La_3Zr_2O_{12}$ has become a strong contender over the years.[6] Not only does this garnet compound present a good Li^+ conductivity,[7,8] it is also stable over a wide electrochemical window[9,10] and provides more stable interfaces with cathode materials,[10] which are key advantages over other promising inorganic electrolytes, such as superionic sulfides. In addition, garnets have higher structural/chemical stability in an air atmosphere than superionic sulfides.[7,8]

$Li_7La_3Zr_2O_{12}$ (LLZ) crystallizes in two polymorphs: a poorly conducting tetragonal phase $I4_1/acd$ (142) at room temper-

Received: December 19, 2016
Revised: January 20, 2017
Published: January 20, 2017

DOI: 10.1021/acs.chemmater.6b05369
Chem. Mater. 2017, 29, 1769−1778

ature and a highly conductive cubic phase $Ia\bar{3}d$ (230) obtained at high temperature (>1273 K).[11] Al^{3+} diffusion from the Al_2O_3 crucible to the garnet structure during thermal treatment has been proven to stabilize the metastable cubic phase[12] *via* disordering of the Li^+ distribution over the available sites (tetrahedral Li_{24d}, octahedral Li_{48g}, and distorted octahedral Li_{96h}, the latter obtained by off-centering the cation in Li_{48g}). As a way to induce crystallization into a cubic system, various substitution strategies, resulting in the creation of Li vacancies, have been studied in recent years.[6] Intentional substitution on the Li^+ sites by Al^{3+} or Ga^{3+} or replacement of Zr^{4+} by M^{5+} cations (M = Nb, Ta) have both proven successful, the latter leading to a nominal composition of $Li_5La_3M_2O_{12}$ in the case of full Zr^{4+} replacement. Substitution performed on the Li site is associated with a rapid decrease of Li content due to the greater charge difference between hosting cation and substituent, leading to the composition $Li_{7-3x}M_xLa_3Zr_2O_{12}$ (M = Al, Ga). Substitution on the Zr site gives finer control over the Li content by adjustment of the M^{5+} level according to the formula $Li_{7-y}La_3Zr_{2-y}M_yO_{12}$ (M = Ta, Nb). Both strategies result in increasing the ratio of $Li_{48g+96h}$:Li_{24d}, which leads to faster ionic conduction, from 10^{-6} to 10^{-4} S cm^{-1} for tetragonal and cubic phases, respectively.[6,11,13] To date, the best ionic conductivity has been achieved for Li substitution by Ga, with a total ionic conductivity (σ_i) of 1.3×10^{-3} S cm^{-1} for $Li_{6.55}Ga_{0.15}La_3Zr_2O_{12}$ and $Li_{6.40}Ga_{0.20}La_3Zr_2O_{12}$ as previously reported by our team and others.[14,15] The high mobility of Li^+ in $Li_{6.55}Ga_{0.15}La_3Zr_2O_{12}$ can be ascribed to the preferential occupancy of Ga^{3+} in the tetrahedral Li_{24d} sites, inducing Li vacancies and thus increasing the ratio of $Li_{48g+96h}$:Li_{24d}.[14]

Molecular dynamics (MD) simulations, reported by Jalem et al.,[16] on Ga substituted LLZ using interatomic potentials predict a very high ionic conductivity, close to 6×10^{-3} S cm^{-1}, for a substitution level of 0.02 mol per formula unit, i.e., n_{Li} = 6.94. However, experimentally it has proven difficult to obtain cubic crystals for $6.55 < n_{Li} \leq 7.0$. The inconsistency between MD and experiments is related to a high sampling temperature (≥1000 K) for the computer simulations, which is above the tetragonal to cubic phase transition temperature (i.e., forcing the structure to be cubic). Experimentally, however, higher Ga substitution levels are needed to stabilize the fast ion-conducting structure at room temperature, with at least 0.15 mol of Ga^{3+}.[14,15] As a consequence of the higher Ga content in the LLZ structure, more Li vacancies are created, thus lowering the total charge carrier concentration. A strategy to partially substitute Zr^{4+} by Y^{3+} has been previously investigated to increase the Li content in $Li_7La_3Zr_2O_{12}$; however, this approach led to compositions with $n_{Li} > 7.0$, which showed a detrimental effect on the ionic conductivity, with values remaining $<10^{-3}$ S cm^{-1} at 300 K.[17,18]

In this paper, a novel dual substitution approach is presented where partial substitution of Li^+ by Ga^{3+} combined to partial substitution of Zr^{4+} by Sc^{3+} gives access to Li compositions with $n_{Li} > 6.55$ while maintaining the cubic structure of LLZ. This strategy has the potential to enhance the ionic conductivity in LLZ. The presence of Ga ensures crystallization in the cubic phase by disordering the Li network over Li_{24d} and Li_{96h} sites via Li_{24d} occupation by Ga^{3+}, while the substitution of Zr^{4+} by a lower valence cation opens a window for fine-tuning of the number of charge carriers according to the resulting formula: $Li_{7-3x+y}Ga_xLa_3Zr_{2-y}Sc_yO_{12}$. Substitution of Zr^{4+} by Sc^{3+} is proposed, instead of Y^{3+} as previously reported in single substituted LLZ.[17,18] Sc^{3+} provides a better ionic radius match with Zr^{4+} (ionic radius for an octahedral coordination of 0.72, 0.75, and 0.90 Å for Zr^{4+}, Sc^{3+}, and Y^{3+}, respectively),[19] ensuring smaller structural distortions in the vicinity of Sc^{3+} compared to Y^{3+}. Additionally, density functional theory (DFT) calculations predict a lower defect energy for scandium over yttrium for the Zr site, yttrium being more prone to be found on the La site.[20] Here, we investigated the effect of dual substitution by Ga and Sc on the crystal structure, microstructure, local cationic distribution, and ionic conductivity of $Li_{7-3x+y}Ga_xLa_3Zr_{2-y}Sc_yO_{12}$ with different substitution levels (x = 0.15 and y = 0.10, 0.15, 0.20). The present study highlights the reasons behind the ionic conductivity enhancement in such dual substituted LLZ garnets, offering new design rules for the development of high-conducting ceramic electrolytes.

METHODS

DFT calculations were performed using a periodic model and the semilocal Perdew–Burke–Ernzerhof (PBE) functional[21] as implemented in the Vienna Ab Initio Simulation Package (VASP, version 5.4.1).[22,23] The inner electrons were replaced by PBE-based projector augmented wave potentials,[24] whereas Li (1s, 2s), La (5s, 5p, 6s, 5d), Zr (4s, 4p, 5s, 4d), O (2s, 2p), Ga (4s, 3d, 4p), and Sc (3s, 3p, 4s, 3d) valence electrons were expanded in plane-waves with a cutoff energy of 520 eV. We used the 8-formula-unit ($Li_7La_3Zr_2O_{12}$) conventional supercell, with cubic symmetry group $Ia\bar{3}d$ (230). The equilibrium lattice parameters of the cell were fixed to the experimental values reported in the ICSD (CC: 422259) by Awaka et al.[25] ($a = b = c$ = 12.9827 Å and $\alpha = \beta = \gamma = 90°$), whereas the internal atomic positions were allowed to relax with a residual force threshold of 0.02 eV $Å^{-1}$. We considered a 2 × 2 × 2 Monkhorst–Pack k-point mesh. These computational settings guarantee a tight convergence in total energies (better than 10 meV per formula unit) and equilibrium distances (better than 0.02 Å). Ga substituted LLZ was modeled by placing one Ga^{3+} per supercell on a Li^+ site ($Li_{53}Ga_1La_{24}Zr_{16}O_{96}$), following the site preference of Ga^{3+} in LLZ computed by Miara et al. using DFT,[20] therefore evaluating two configurations, one with Ga^{3+} in tetrahedral Li_{24d} and the second one with Ga^{3+} in octahedral $Li_{48g/96h}$. In the case of the dual substituted system, we replaced one Zr atom per supercell by one Sc atom in the presence of one Ga^{3+} again on a Li^+ site ($Li_{54}Ga_1La_{24}Zr_{15}Sc_1O_{96}$, with 0.125 mol of Sc). We considered all 32 possible arrangements of Ga^{3+} and Sc^{3+} within the supercell, involving the 16 different Zr^{4+} sites, with Ga^{3+} either in a tetrahedral Li_{24d} or octahedral $Li_{48g+96h}$ site. Notice that the disordered nature of Li^+ sites in the pristine and doped cubic garnet structures results in a very large number of possible Li^+ and Li^+ vacancy arrangements within the Li sublattice. Therefore, we applied a screening procedure by first computing the electrostatic energy using formal charges and the Ewald summation.[26] In order to improve the efficiency in the sampling of low-energy states, we considered only atomic arrangements with no Li–Li pairs at distances lower than 1 Å. We evaluated a total of 200 000 random Li arrangements, with no restriction in the partial occupancies of tetrahedral and octahedral sites. We then computed the energies of the 10–20 lowest electrostatic energy structures using DFT. In the dual substituted system, we applied this procedure for each of the 32 Ga^{3+}–Sc^{3+} configurations. Similar two-step screening procedures have recently been applied to account for disordered Li site occupancy in garnets[16,20] and other solids.[27]

$Li_{7-3x+y}Ga_xLa_3Zr_{2-y}Sc_yO_{12}$ samples (x = 0.15 and y = 0.10, 0.15, and 0.20) were prepared by a sol–gel route using $LiNO_3$ (Reagent plus, Sigma-Aldrich), Ga_2O_3 (99.99%, Aldrich), $La(NO_3)_3{\cdot}6H_2O$ (> 99.0%, Fluka), $Zr(C_5H_7O_2)_4$ (Alfa Aesar), and Sc_2O_3 (99.9%, Aldrich) as starting reagents. Prior to the reaction, Ga_2O_3 was digested in a 65% HNO_3 solution via a 2 h microwave treatment to ensure full dissolution of the gallium cations, leading to a final Ga^{3+} concentration of 0.02 mol L^{-1}. Stoichiometric amounts of starting materials—with a 10% $LiNO_3$ excess to compensate for Li evaporation during the sintering phase—were placed in a porcelain dish. Citric acid (> 99.0%, Sigma-Aldrich) previously dissolved in a minimum amount of distilled

DOI: 10.1021/acs.chemmater.6b05369
Chem. Mater. 2017, 29, 1769–1778

water was added to the reagents mixture, with a citric acid to cation ratio of 4:1. After dissolution, the solution was dehydrated on a hot plate, and the resulting gel was then annealed at 873 K for 12 h to decompose the organic components. The resulting powder was ground and heated to 1073 K for 12 h under a dry O_2 atmosphere (H_2O content < 1 ppm). After this thermal treatment, the calcined powder was quickly transferred to an argon-filled glovebox (H_2O content < 0.1 ppm and O_2 content < 0.6 ppm) for further grinding. The powder was then pressed at 2 tons into pellets with a 1/4 in. diameter. The pellets were buried in their mother powder and sintered at 1473 K for 6 h under dry O_2 atmosphere (H_2O content < 1 ppm). After the final thermal treatment, the pellets were quickly transferred to an argon-filled glovebox (H_2O content < 0.1 ppm and O_2 content < 0.6 ppm). Both thermal treatments were performed in Al_2O_3 crucibles. After sintering, the pellets were polished to a mirror-like finish with silicon carbide polishing disks of successively smaller grit down to P4000. Their geometrical dimensions and weight were measured to estimate the relative density of the samples based on a theoretical density of 5.11 g cm^{-3}.

X-ray diffraction (XRD) was performed after grinding the pellets in an argon-filled glovebox with an air-protected sample holder with a Be window. A Bruker-D8 diffractometer using a Cu source with Kα1 and Kα2 (accelerating voltage of 30 kV and current of 50 mA) was used in the Bragg–Brentano geometry; the data were collected for 2Θ angles from 15 to 80° with a 0.02° step size. Refinements of the spectra and lattice parameter calculation were performed using the WinPlotr/FullProf package.[28] The peak shape was described by a pseudo-Voigt function and the background level was modeled using a polynomial function.

Elemental analysis was performed using a Horiba Ultima2 inductively coupled plasma optical emission spectrometer (ICP-OES) after digestion of the samples in ultrapure HNO_3 acid (30% concentration, trace metal grade, Fischer Scientific) via a microwave treatment (400 W, 463 K, 1 h) and subsequent dilution in deionized water (Millipore, registering 13.1 MΩcm at 298 K).

The microstructure of the pellet cross section was analyzed by scanning electron microscopy (SEM) using a FEI Quanta 200 FEG operated at a voltage of 30 kV. Elemental composition of local areas was acquired using energy dispersive X-ray spectroscopy (EDS). The pellets were gently broken in an argon-filled glovebox and quickly transferred to the SEM chamber to minimize air exposure. To reveal the grain shape and boundaries, a thermal etching was performed on the broken pellets after fine polishing of the cross section. The pellet pieces were taken to 1423 K for 10 min followed by quenching; the procedure was achieved under an Ar atmosphere. EDS analysis was also performed in scanning transmission electron microscopy (STEM) mode by applying a FEI G2 TEM, operated at 200 kV. Pieces of the pellets were thoroughly ground under an argon atmosphere in order to analyze single particles. Some powder was then mixed with ethanol, and a drop of the solution was deposited on top of the carbon film supported by the copper grid. The grid was then heated at 473 K for 5 min to evaporate the ethanol.

All magic angle spinning nuclear magnetic resonance (MAS NMR) spectra were recorded with a Bruker Avance III 500 MHz (11.7 T) spectrometer working at Larmor frequencies of 500.24, 194.41, 152.56, 130.35, and 121.52 MHz for ^{1}H, ^{7}Li, ^{71}Ga, ^{27}Al, and ^{45}Sc, respectively. Rotors with a diameter of 1.3 mm were packed inside a glovebox with air-unexposed powdered samples. The MAS frequency was set to 50 kHz in all cases. ^{7}Li, ^{71}Ga, ^{27}Al, and ^{45}Sc spectra were referenced to 0.1 M LiCl, $Ga(NO_3)_3$, $Al(NO_3)_3$, and $Sc(NO_3)_3$ solutions, respectively, and ^{1}H shifts were referenced to a bulk water sample resonating at 4.8 ppm. The nonselective $\pi/2$ pulse durations were 4.0, 2.5, 1.3, 1.3, and 1.5 μs for ^{1}H, ^{7}Li, ^{71}Ga, ^{27}Al, and ^{45}Sc, respectively. ^{1}H echo experiments were carried out, and the magnetization observed in empty rotor measurements was subtracted from the sample measurements in order to suppress background signals. Single pulse experiments were performed for the other nuclei. Recycle times of 3, 35, 1, 1, and 7 s for ^{1}H, ^{7}Li, ^{71}Ga, ^{27}Al, and ^{45}Sc along with 16, 16, 149 136, 7712, and 5120 scans accumulated, respectively. The DMFIT[29] software was used to reconstruct and simulate the spectra.

In order to measure the ionic conductivity of the samples, the finely polished pellets with a thickness of 1 mm were assembled in CR2032 coin cells using two Li metal electrodes under an argon atmosphere. Electrochemical impedance spectroscopy (EIS) was performed on the cells using a Solartron 1260A Impedance Analyzer and Z-plot software with a frequency range of 10 MHz to 1 Hz and a signal amplitude of 50 mV. The EIS spectra were normalized using the surface area and thickness of each pellet and fitted to an equivalent circuit (Supporting Information Figure S10) using the Z-view software. To determine the activation energy of each sample, EIS measurements were performed over a temperature range of 180 to 340 K using a physical property management system (PPMS) and the CR2032 coin cells with Li electrodes. The ionic conductivity of each sample over the temperature range was plotted versus $1/T$ in order to extract the activation energy, E_a, according to the following equation:

$$\sigma T = A \exp(-E_a/RT) \quad (1)$$

RESULTS AND DISCUSSION

The dual substitution strategy reported here can be described by the following crystal-chemistry (defect) reactions, using Kröger–Vink notations:

$$Ga_2O_3 \xrightarrow{Li_2O} 2Ga_{Li}^{\bullet\bullet} + 3O_O^x + 4V'_{Li} \quad (2)$$

$$Sc_2O_3 + Li_2O + 2V'_{Li} \xrightarrow{ZrO_2} 2Sc'_{Zr} + 2Li_{Li}^x + 4O_O^x \quad (3)$$

With an overall resulting reaction of

$$Ga_2O_3 + Sc_2O_3 + Li_2O \xrightarrow{Li_2O,ZrO_2} 2Ga_{Li}^{\bullet\bullet} + 2Sc'_{Zr} + 2Li_{Li}^x + 7O_O^x + 2V'_{Li} \quad (4)$$

where $Ga_{Li}^{\bullet\bullet}$ indicates a Ga^{3+} at a Li^+ site with an effective charge of +2, Sc'_{Zr} indicates a Sc^{3+} at a Zr^{4+} site with an effective charge of −1, Li_{Li}^x indicates a Li^+ at a Li site with a neutral charge, O_O^x is an O at the O site with a neutral charge, and V'_{Li} represents a vacancy at a Li^+ site with an effective charge of −1.

In $Li_{7-3x+y}Ga_xLa_3Zr_{2-y}Sc_yO_{12}$, the substitution of x moles of Ga^{3+} on Li^+ sites leads to the creation of $2x$ moles of Li vacancies, which helps disordering the Li population over Li_{24d} and $Li_{48g+96h}$ sites but decreases the number of moles of Li by $3x$. Simultaneously, substitution of y moles of Zr^{4+} by Sc^{3+} allows fine-tuning of the number of Li^+ charge carriers by an incorporation of y moles of Li^+.

We first used DFT calculations to investigate the effect of the proposed dual substitution strategy on the garnet structure. In the (Sc-free) supercell $Li_{53}Ga_1La_{24}Zr_{16}O_{96}$ ($n_{Ga\text{-per-formula-unit}}$ = 0.125), the DFT results indicate that Ga ions in tetrahedral Li_{24d} sites are 161 meV per formula unit more stable than Ga in $Li_{48g+96h}$, in agreement with our previous experimental results.[14] The additional partial substitution of Zr by Sc leads to 32 possible arrangements of Ga and Sc in the supercell $Li_{54}Ga_1La_{24}Zr_{15}Sc_1O_{96}$ ($n_{Ga\text{-per-formula-unit}}$ = 0.125 and $n_{Sc\text{-per-formula-unit}}$ = 0.125). The ground state crystal structure shows the presence of Sc on Zr sites and Ga on Li_{24d} sites (Figure 1a). The relative stability of other computed structures is represented as a function of the Ga–Sc distance in Figure 1b. Our results clearly indicate a preference of Ga^{3+} in tetrahedral Li_{24d} sites, with the first Ga in the $Li_{48g+96h}$ site appearing 139 meV per formula unit higher in energy than the ground state. This energy difference is 22 meV per formula unit lower than the one found in the case of Sc-free supercells. This suggests that the dual substituted system shows a slightly larger tendency toward Ga populating $Li_{48g/96h}$ sites than the Sc-free

DOI: 10.1021/acs.chemmater.6b05369
Chem. Mater. 2017, 29, 1769–1778

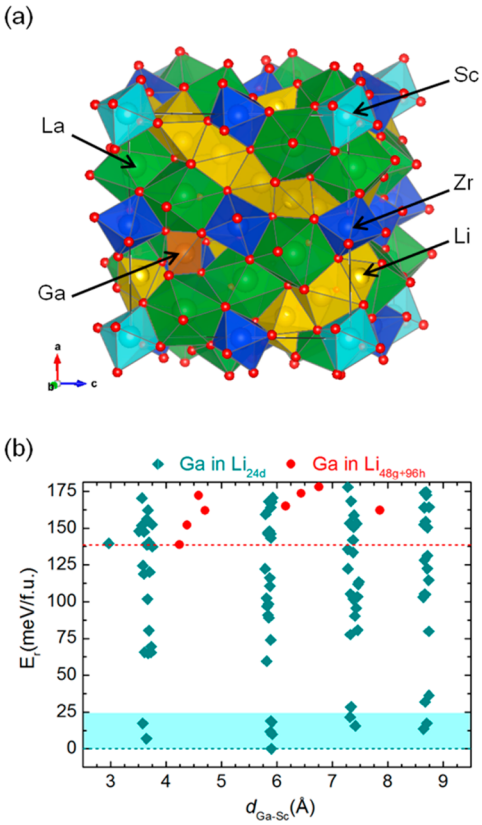

Figure 1. DFT simulations of dual substituted LLZ garnet. (a) Polyhedral representation of the lowest energy $Li_{54}Ga_1La_{24}Zr_{15}Sc_1O_{96}$ unit cell with Li, Ga, La Zr, Sc, and O ions shown in yellow, orange, green, blue, turquoise, and red, respectively. (b) Relative energy E_r of the unit cell $Li_{54}Ga_1La_{24}Zr_{15}Sc_1O_{96}$, with Ga in Li_{24d} tetrahedral sites (turquoise data points) and with Ga in $Li_{48g+96h}$ octahedral sites (red data points), as a function of Ga−Sc distance (d_{Ga-Sc}). Each point corresponds to a DFT calculation of a Ga−Sc configuration with a given Li^+ arrangement. The turquoise (red) dotted line indicates the ground-state configuration for Ga in Li_{24d} ($Li_{48g+96h}$). All energies are referenced to the total energy of the ground state for Ga in Li_{24d}. The light blue band highlights Ga in Li_{24d} structures at different Ga−Sc distances with relative energies within a range of less than 15 meV per formula unit compared to the ground state.

system. Interestingly, it is also found that the presence of Sc has a weak impact on the Ga distribution: the lowest-energy structures with Ga in Li_{24d} for each of the four groups of Ga−Sc distances (~3.6 Å, ~5.9 Å, ~7.4 Å, and ~8.7 Å) are within less than 15 meV per formula unit (light blue band in Figure 1b).

XRD and Rietveld refinements of $Li_{6.55+y}Ga_{0.15}La_3Zr_{2-y}Sc_yO_{12}$ with y = 0.10 (LGLZ_Sc10), 0.15 (LGLZ_Sc15), and 0.20 (LGLZ_Sc20) confirm crystallization in a cubic phase with space group $Ia\bar{3}d$ (230) for all three compositions (Figure 2a and Supporting Information Figure S1). Upon increasing the Sc substitution level, the Bragg reflections shift to lower 2θ (Figure 2b), and the lattice parameter extracted from Rietveld refinements increases linearly following Vegard's law, with 12.970(2), 12.976(1), and 12.984(2) Å for LGLZ_Sc10, LGLZ_Sc15, and LGLZ_Sc20, respectively (Figure 2c). This confirms the formation of a solid solution with substitution of some Zr^{4+} cations (0.72 Å) by larger Sc^{3+} ions (0.75 Å) in the garnet crystal structure. A trace amount of $LiScO_2$ was also detected (Figure 2a and Supporting Information Figure S1).

Geometrical density measurements of the sintered pellets indicate high density for all three compositions with 93%, 93%, and 94% for LGLZ_Sc10, LGLZ_Sc15, and LGLZ_Sc20, respectively. In agreement, cross-sectional SEM imaging shows only a limited number of pores remaining in the pellets (Figure 3a,b). The porosity represents 2 to 3% of the observed areas with a mean diameter of 3 to 4 μm. Thermal etching of the sample with LGLZ_Sc15 reveals the presence of a wide array of grain sizes ranging from ~5 to ~70 μm (Figure 3c). Backscattering imaging of the three cross-sections (Supporting Information Figure S2) discloses the presence of a secondary phase containing lighter elements (due to its darker contrast), its ratio increasing with Sc content. This could correspond to the small amount of $LiScO_2$ observed by XRD.

The stoichiometry of the dual substituted garnet samples was confirmed by using a combination of analytical techniques: ICP, SEM-EDS, and STEM-EDS (Table 1).

ICP characterization of the overall sample composition indicated a Zr/La ratio slightly higher than expected, while the ratios of Ga/La and Sc/La are those expected. Only a small amount of Al is detected, indicating minor contamination during thermal treatment of the samples in Al_2O_3 crucibles,[12,30] the Al/La ratio being well below the one required for cubic stabilization of the garnet by Al (0.068).[31]

The chemical composition of local regions of the pellets was analyzed by SEM-EDS. The metal ratio values shown in Table 1 are extracted from averaging over several locations of the LGLZ_Sc region. These analyses confirm that the LGLZ_Sc regions contain the expected amount of Ga for all samples. The Sc content linearly increases with the substitution level in the garnet region (with y = 0.07, 0.08, and 0.09 for LGLZ_Sc10, LGLZ_Sc15, and LGLZ_Sc20, respectively). This value is slightly below the total amount of Sc measured by ICP (y = 0.09, 0.12, and 0.18 for LGLZ_Sc10, LGLZ_Sc15, and LGLZ_Sc20, respectively). The Zr concentration in the garnet region is also lower than expected for all samples. The missing Sc and Zr cations are both encountered in the secondary phase (Supporting Information Figure S3 and Table S1), which would be best described as Zr substituted $LiScO_2$. This phase probably acts both as a reaction intermediate and as a sintering aid during thermal treatment of the garnet and would explain the high density of the obtained pellets.

Finally, single-particle STEM-EDS measurements were also performed on LGLZ_Sc20 and confirmed the presence of both Ga and Sc within the LGLZ_Sc grains (Table 1, Figure 3d, and Supporting Information Figure S4). Only a trace amount of Al was detected, suggesting its segregation at the grain boundary, and thus not affecting the stoichiometry of the dual substituted garnet. STEM-EDS analysis on a grain of the secondary phase confirms its previous assignment to a Zr substituted $LiScO_2$ phase (Supporting Information Table S1 and Figure S4).

Next, a thorough solid state NMR study has been carried out on the dual substituted garnets (LGLZ_Sc10 and LGLZ_Sc20) to identify the local cationic distribution and to assess the local Li^+ mobility. All samples were carefully handled in a glovebox to avoid Li^+−H^+ exchange (protonation), as confirmed by the absence of peaks in ^1H NMR (Supporting Information Figure S5).

^{71}Ga NMR of LGLZ_Sc10 shows the presence of a single Ga resonance with a distinctive second order quadrupolar broadening (Figure 4a). This resonance is reminiscent of the one observed in single substituted $Li_{6.55}Ga_{0.15}La_3Zr_2O_{12}$[14] and can therefore be assigned to Ga^{3+} in tetrahedral Li_{24d} sites. The

DOI: 10.1021/acs.chemmater.6b05369
Chem. Mater. 2017, 29, 1769−1778

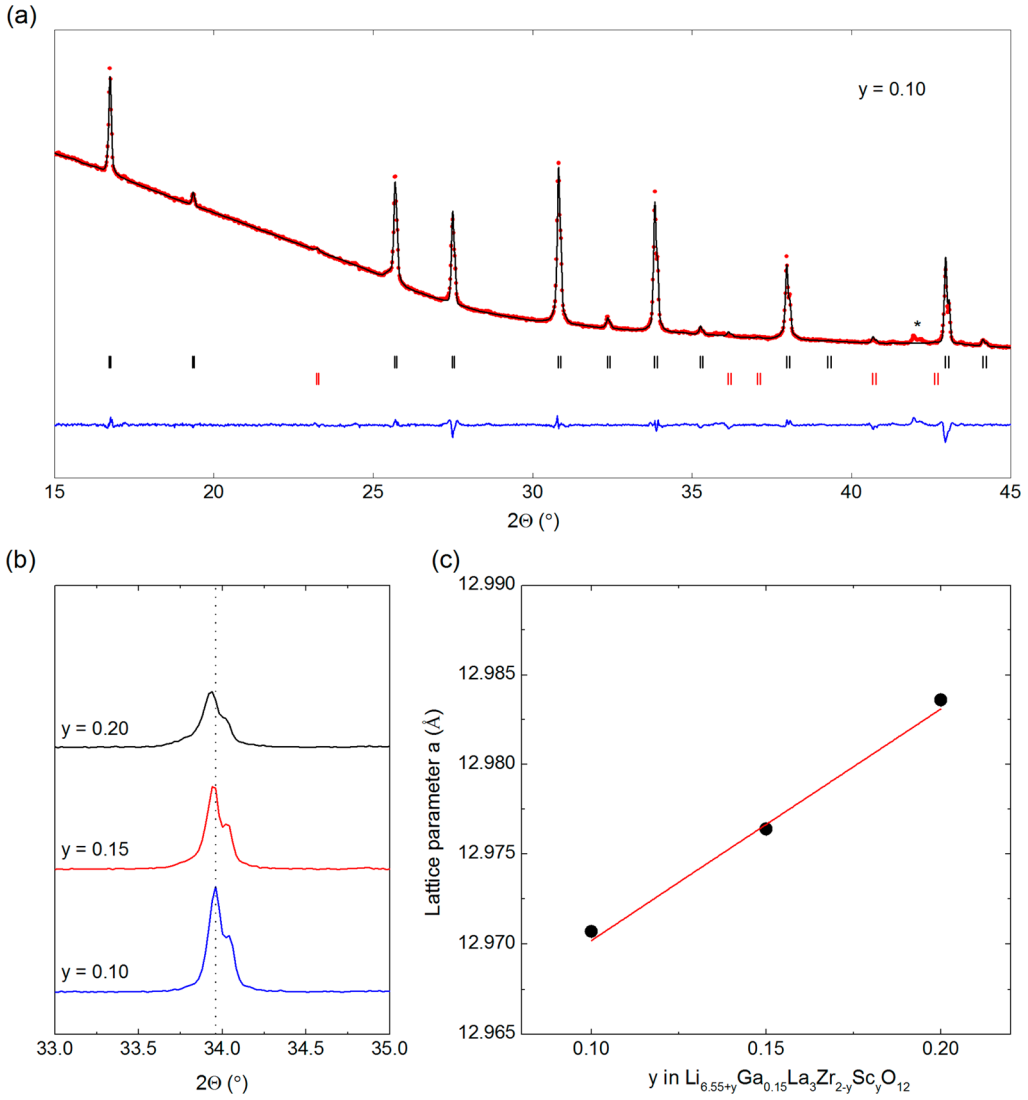

Figure 2. XRD characterization of the dual substituted garnet $Li_{6.55+y}Ga_{0.15}La_3Zr_{2-y}Sc_yO_{12}$. (a) Rietveld refinement for $y = 0.10$. The asterisk denotes contribution from the sample holder, and the bars in black and red below the profile represent the Bragg peak positions associated with the cubic garnet phase and traces $LiScO_2$, respectively. (b) Details of the (422) reflection showing the peak shift upon Sc substitution. (c) Change of the cubic lattice parameter, *a*, upon Sc substitution (the error bars are smaller than the points).

same resonance appears in LGLZ_Sc20, though a second signal is also observed at 240 ppm, which shift and line shape can be ascribed to Ga cations with a distorted octahedral Li_{96h} environment as reported in analogous garnet materials.[32,33] Therefore, it can be concluded that, at low Sc content (y = 0.10), the preferred atomic sites for Ga^{3+} are the tetrahedral Li_{24d} sites and, at higher Sc content (y = 0.20), Ga^{3+} can also populate the distorted octahedral Li_{96h} sites.

The ^{45}Sc NMR spectra of LGLZ_Sc10 and LGLZ_Sc20 are very similar, with a higher signal intensity for the latter in agreement with the sample composition (Figure 4b). Spectral deconvolution allowed the identification of two Sc signals (Supporting Information Figure S6): a main signal is observed at 140 ppm with a weaker contribution at about 120 ppm. The resonance at 140 ppm falls in the range of expected shifts for 6-coordinated Sc cations (100−160 ppm).[34] On the one hand, substitution of octahedral Zr^{4+} by Sc^{3+} in $BaZr_{1-y}Sc_yO_3$ led to a similar ^{45}Sc signal with a shift of 140 ppm.[35] On the other hand, $LiScO_2$ presents a comparable line shape but with a chemical shift value of 148 ppm,[34] slightly higher than the one of the observed species. However, substitution of Sc^{3+} by Zr^{4+} in $LiScO_2$ could lead to a slight decrease of its chemical shift, as observed in the $BaZr_{1-y}Sc_yO_3$ series,[35] in which case it would be difficult to separate its contribution from that of Sc in the LLZ phase. The quadrupolar constant of the resonance observed at 140 ppm is small, indicating a highly symmetric octahedral distribution of cations in the surroundings of Sc^{3+}. It reveals minimal geometrical distortion related to the partial substitution of Zr^{4+} by Sc^{3+} as expected from the low strain owing to similar ionic radii between the two cations (0.72 and 0.75 for Zr^{4+} and Sc^{3+}, respectively, in octahedral environment).[19] The weak resonance observed at 120 ppm is reminiscent of Sc_2O_3[34−36] and could result from a trace amount of undissolved Sc precursor reagent during solution mixing, below the detection limit of XRD. Prior dissolution of Sc_2O_3 via acid digestion could facilitate homogenization of the initial solution in future work.

^{27}Al NMR of the dual substituted samples shows two resonances, at 62 and 78 ppm (Supporting Information Figure S7). On the basis of prior studies,[12,37−40] they are respectively

DOI: 10.1021/acs.chemmater.6b05369
Chem. Mater. 2017, 29, 1769−1778

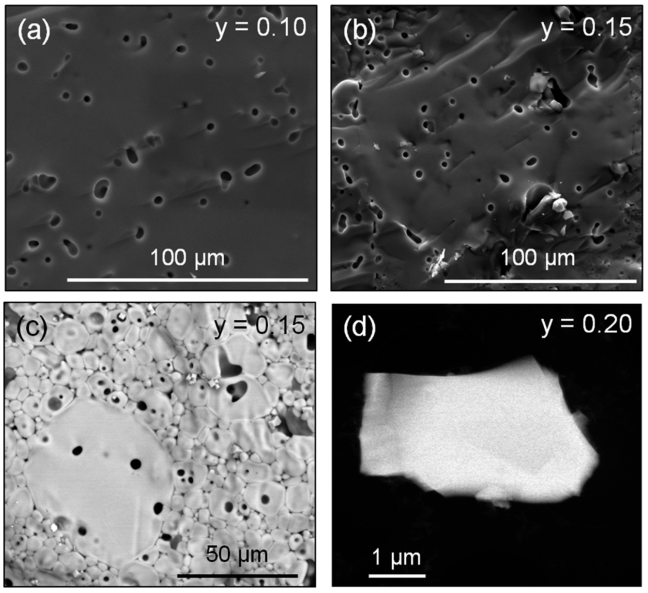

Figure 3. Cross-sectional SEM images of sintered pellets of $Li_{6.55+y}Ga_{0.15}La_3Zr_{2-y}Sc_yO_{12}$ with composition (a) y = 0.10 and (b) y = 0.15. (c) Backscattered electron microscopy of thermally etched pellet with y = 0.15. (d) STEM image of a single particle for y = 0.20.

assigned to Al^{3+} in tetrahedral Li_{24d} and in distorted octahedral Li_{96h} sites, the latter having a locally 4-fold coordination based on its chemical shift.[41−43] In conclusion, ^{27}Al NMR confirms the presence of some Al in the dual substituted samples, most likely located at the grain boundary of the LLZ regions as concluded from the ICP and SEM-EDS results.[12]

Regarding the ^7Li NMR, the spectra of both LGLZ_Sc10 and LGLZ_Sc20 show similar chemical shifts but variations in line width, especially when compared to single substituted garnet $Li_{6.55}Ga_{0.15}La_3Zr_2O_{12}$ (Figure 4c).[14] Deconvolution of the ^7Li NMR spectra of the dual substituted garnets reveals the presence of at least two resonances, with a broader line width for LGLZ_Sc10 (Supporting Information Figure S8). This broadening highlights a larger distribution of chemical environments in LGLZ_Sc10 with more local disorder surrounding the Li cations, in sharp contrast with the narrow peak of single substituted garnets (Figure 4c).

The observed differences in the Li local structure are expected to influence the transport properties of the dual substituted garnets. To evaluate the Li-ion dynamics at the local scale, we performed saturation recovery experiments (Supporting Information Figure S9). A multiexponential behavior in the Li spin−lattice relaxation times (T_1) for the dual substituted samples further reveals the presence of a heterogeneous distribution of Li environments (Table 2 and Supporting Information Figure S9). Fitting of the relaxation curves indicates the existence of a Li population with a T_1 value lower (< 0.20 s) than in single substituted $Li_{6.55}Ga_{0.15}La_3Zr_2O_{12}$ (0.38 s) garnet.[14] This difference could suggest faster Li^+ hopping rates for part of the Li population in the dual substituted samples, although quantification of the individual activation energies by longitudinal relaxation measurements requires a complete NMR spin−lattice relaxation study with temperature and frequency-dependent measurement of the spin−lattice relaxation rates in the laboratory and rotating frames.[44]

Solid state NMR gives valuable information on the Li-ion dynamics, but only on a local scale. Thus, to evaluate the effect of the dual substitution strategy on the macroscopic transport properties, electrochemical impedance spectroscopy (EIS) measurements were performed at various temperatures. Nyquist plots (Figure 5a) of dual substituted LGLZ pellets recorded at 300 K show two semicircles, the one at high frequency being representative of the total ionic conductivity (bulk + grain boundary) of the pellet and the one at low frequency arising from the interfacial resistance between the pellet and the Li electrodes. The total ionic conductivity at 300 K (Figure 5b) is calculated for each composition by fitting the Nyquist plots with a circuit model previously described[14] (Supporting Information Figure S10) and taking into consideration the pellet dimensions. As a result of the dual substitution, the ionic conductivity increases from 1.1(1) × 10^{-3} S cm^{-1} for the Sc-free sample to an optimal value of 1.8(4) × 10^{-3} S cm^{-1} for LZLG_Sc10 ($Li_{6.65}Ga_{0.15}La_3Zr_{1.90}Sc_{0.10}O_{12}$), proving the beneficial effect of the Sc and representing a new maximum for garnet electrolytes: 1.8 × 10^{-3} S cm^{-1} at 300 K. This conductivity value is in the range of the one predicted by Matsui et al.[45] for a cubic $Li_7La_3Zr_2O_{12}$ based on extrapolation of their high temperature

Table 1. Expected Chemical Composition and Experimental Metal Ratios of the As-Prepared Samples Determined by ICP, SEM-EDS, and STEM-EDS Techniques[a]

composition	Zr/La	Ga/La	Sc/La	Al/La
Expected				
$Li_{6.65}Ga_{0.15}La_3Zr_{1.90}Sc_{0.10}O_{12}$	0.633	0.050	0.033	0.000
$Li_{6.70}Ga_{0.15}La_3Zr_{1.85}Sc_{0.15}O_{12}$	0.617	0.050	0.050	0.000
$Li_{6.75}Ga_{0.15}La_3Zr_{1.80}Sc_{0.20}O_{12}$	0.600	0.050	0.067	0.000
ICP				
$Li_{6.65}Ga_{0.15}La_3Zr_{1.90}Sc_{0.10}O_{12}$	0.674(2)	0.053(6)	0.031(0)	0.010(1)
$Li_{6.70}Ga_{0.15}La_3Zr_{1.85}Sc_{0.15}O_{12}$	0.678(47)	0.050(2)	0.039(2)	0.032(2)
$Li_{6.75}Ga_{0.15}La_3Zr_{1.80}Sc_{0.20}O_{12}$	0.704(9)	0.060(3)	0.060(1)	0.007(2)
SEM-EDS				
$Li_{6.65}Ga_{0.15}La_3Zr_{1.90}Sc_{0.10}O_{12}$	0.49(9)	0.055(3)	0.024(2)	0.09(1)
$Li_{6.70}Ga_{0.15}La_3Zr_{1.85}Sc_{0.15}O_{12}$	0.47(7)	0.061(5)	0.026(3)	0.089(1)
$Li_{6.75}Ga_{0.15}La_3Zr_{1.80}Sc_{0.20}O_{12}$	0.45(6)	0.062(4)	0.029(1)	0.053(8)
STEM-EDS				
$Li_{6.75}Ga_{0.15}La_3Zr_{1.80}Sc_{0.20}O_{12}$	0.71(5)	0.061(11)	0.023(6)	<0.005

[a]The given errors are experimental for ICP and statistical for SEM-EDS and STEM-EDS results.

DOI: 10.1021/acs.chemmater.6b05369
Chem. Mater. 2017, 29, 1769−1778

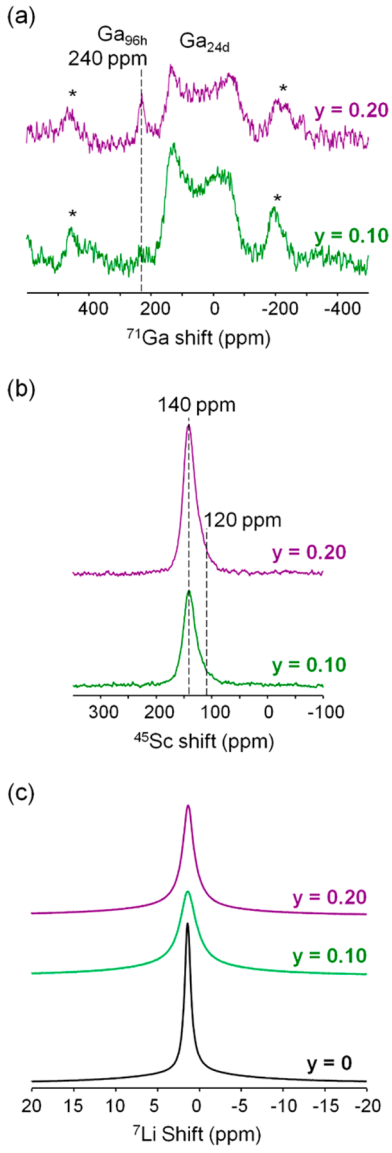

Figure 4. Solid state NMR spectra of $Li_{6.55+y}Ga_{0.15}La_3Zr_{2-y}Sc_yO_{12}$: (a) ^{71}Ga, (b) ^{45}Sc, and (c) ^{7}Li. The asterisks in part a denote the spinning sidebands of the broad quadrupolar resonance. The single substituted $Li_{6.55}Ga_{0.15}La_3Zr_2O_{12}$ sample in part c is shown for comparison.[14]

Table 2. T_1 Relaxation Times for ^{7}Li Extracted from Saturation Recovery Experiments (Supporting Information Figure S9) of $Li_{6.55+y}Ga_{0.15}La_3Zr_{2-y}Sc_yO_{12}$

y	component	contribution (%)	T_1 (s)
0	A	100	0.38
0.10	A	50	0.36
	B	50	0.15
0.20	A	50	0.42
	B	50	0.17

data (1.7×10^{-3} S cm^{-1}). A further increase in Sc content leads to a decrease in ionic conductivity with 1.0(2) and 0.5(1) $\times$ 10^{-3} S cm^{-1} for LGLZ_Sc15 and LGLZ_Sc20, respectively.

In accordance to the ionic conductivity enhancement, the activation energy E_a extracted from the Arrhenius plots (Figure 5c) decreases in the dual substituted garnets. E_a lowers from 0.31 for the Sc-free sample to 0.29 eV for y = 0.10 in $Li_{6.55+y}Ga_{0.15}La_3Zr_{2-y}Sc_yO_{12}$ (Figure 5d). The same minimum is observed for y = 0.15 before increasing back to 0.31 eV for y = 0.20. Therefore, the fastest ionic conductivity observed for y = 0.10 is combined with the lowest activation energy, representing the optimal Sc content to achieve faster ion transport in these dual substituted garnets.

The ionic conductivity enhancement observed for the dual substituted $Li_{6.65}Ga_{0.15}La_3Zr_{1.90}Sc_{0.10}O_{12}$ cannot be associated with a possible Al contamination, as Al substituted $Li_7La_3Zr_2O_{12}$ garnets typically show much lower ionic conductivities, with $\sigma_i \leq 5 \times 10^{-4}$ S cm^{-1}.[30,31] It is possible that the higher ionic conductivity of LGLZ_Sc10 arises from higher densification of the pellet; a similar effect has been reported in $Li_{5+2x}La_3Nb_{2-x}Sc_xO_{12}$ on Sc substitution.[46] It could also be related to the presence of the Zr substituted $LiScO_2$ secondary phase, known to offer some (limited) ionic conductivity.[47]

However, the previous hypotheses cannot stand as the sole explanations for the ionic conductivity enhancement. Indeed, analysis of the Li populations by ^{7}Li NMR in the dual substituted samples highlights clear differences compared to the Sc-free sample. While all samples host a Li population with a relaxation time in the range of 0.38(2) s, the dual substituted samples accommodate a second population of Li^+ with a shorter relaxation time—of 0.16(1) s—hinting toward the presence of Li^+ with faster local motion. It is also associated with a decrease in activation energy observed for LGLZ_Sc10 and LGLZ_Sc15 (0.29 eV versus 0.31 eV for LGLZ), the activation energy reflecting on local energy barriers for Li-ion migration. Nevertheless, faster local motion is not necessarily correlated to faster long-range mobility as local cationic distribution may influence the long-range diffusion. This hypothesis could explain the decrease of ionic conductivity observed upon further Sc substitution in LGLZ_Sc15 and LGLZ_Sc20, the latter showing some occupation of Ga^{3+} in the octahedral Li sites, as opposed to the preferential occupation of the tetrahedral Li sites at lower Sc content (y = 0.10).

The proposed dual substitution strategy, $Li_{6.55+y}Ga_{0.15}La_3Zr_{2-y}Sc_yO_{12}$, leads to a very particular cationic distribution. For low substitution levels, Ga^{3+} is found in the tetrahedral Li_{24d} sites, as suggested by our DFT calculations. The smaller ionic radius of Ga^{3+} makes it a preferential occupant of the Li_{24d} sites over Li_{96h} sites (0.47 and 0.59 Å for Ga^{3+} and Li^+, respectively, in a tetrahedral coordination).[19] The addition of Sc leads to a larger number of local environments for Li^+, which increases the local disorder surrounding the charge carrier and therefore its local mobility. For high Sc contents (y = 0.20), the amount of Ga in tetrahedral Li_{24d} decreases slightly and is compensated by the presence of some Ga^{3+} on the distorted octahedral Li_{96h} sites. This occupation of the Li_{96h} sites appears to have a negative impact on the long-range Li^+ mobility.

Overall, the limited occupation of Li_{96h} sites by cations other than Li^+ combined with the presence of a larger distribution of Li environments could explain the better performances of the dual substituted sample $Li_{6.65}Ga_{0.15}La_3Zr_{1.90}Sc_{0.10}O_{12}$ over the single substituted $Li_{6.55}Ga_{0.15}La_3Zr_2O_{12}$. These findings support the prior hypothesis from Thompson et al.,[13] which stated that a further increase in ionic conductivity could be expected for n_{Li} > 6.5, not by generally increasing the concentration of Li^+ in the garnet but by selectively increasing the ratio of Li_{96h}/Li_{24d}.

It is worth noting that Ga site occupancy in our samples (this study and our previous work[14]) is different from other reported studies.[32,33] At low substitution levels, we observe Ga in Li_{24d}

DOI: 10.1021/acs.chemmater.6b05369
Chem. Mater. 2017, 29, 1769−1778

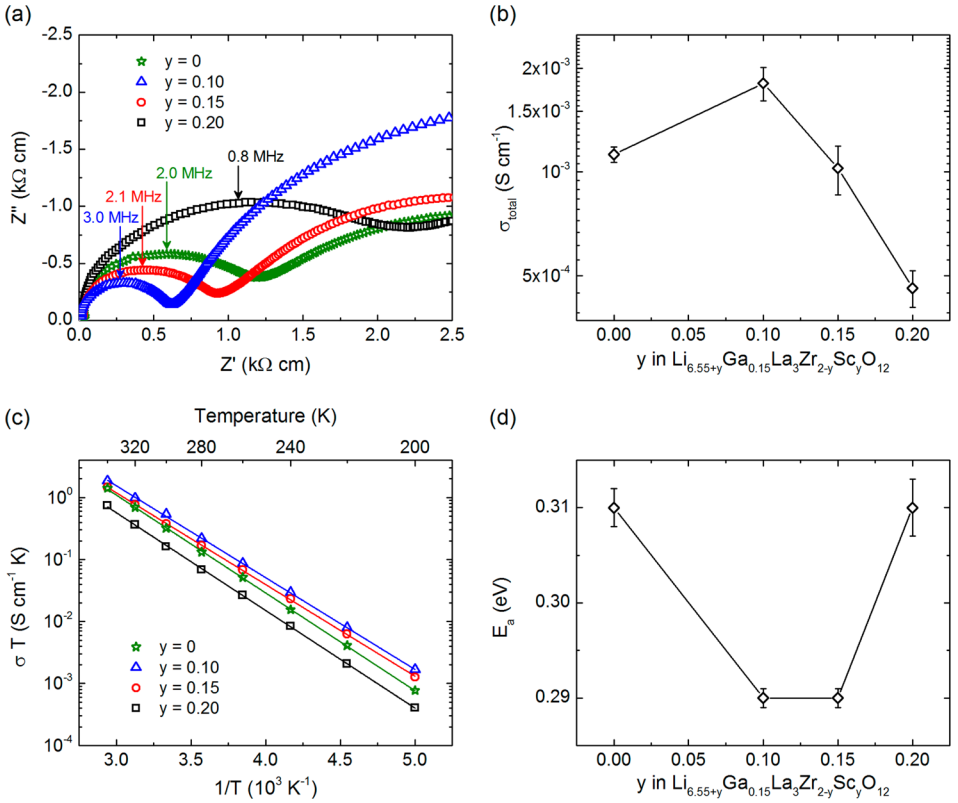

Figure 5. Electrochemical impedance characterization of $Li_{6.55+y}Ga_{0.15}La_3Zr_{2-y}Sc_yO_{12}$ for y = 0.10, 0.15, and 0.20: (a) Nyquist plots at 300 K, (b) total ionic conductivity at 300 K, (c) Arrhenius plots, and (d) extracted activation energy E_a at various doping levels. The y = 0 data values were added for comparison. All measurements were performed using two Li metal electrodes in coin cell configuration.

preferentially, with Li_{96h} occupation on further substitution, while other studies found Ga to systematically occupy Li_{96h} even at a low Ga substitution level.[32] Those discrepancies could be related to the sample preparation and/or the sample composition. In the present study, the as-prepared garnets are synthesized in an ultradry atmosphere (O_2 flow with < 1 ppm of H_2O for calcination and sintering steps and material handling performed in an argon glovebox), while other works processed the samples in air.[32,33] The latter processing is often characterized by a poorly connected network of small grains (≈ 10 μm), which typically leads to lower ionic conductivity and higher activation energy. Unfortunately, impedance measurements were not performed in those studies, and direct comparison of ionic conductivity based on cationic distribution cannot be proposed. In such a case, sample preparation in a dry atmosphere should be considered as it would allow further comparison as well as leading to higher conductivity. Additionally, a smaller amount of substitution could possibly favor occupancy of Li_{24d} sites by Al^{3+} and/or Ga^{3+} over Li_{96h} sites based on the smaller ionic radii of Al^{3+} and Ga^{3+} compared to Li^+. This hypothesis is corroborated by the latest contribution of Rettenwander et al.,[15] where neutron powder diffraction and single crystal diffraction of $Li_{6.4}Al_{0.2-x}Ga_xLa_3Zr_2O_{12}$ compositions did not show Al or Ga occupancy of Li_{96h} sites and led to a conductivity of 1×10^{-3} S cm^{-1} at 295 K for x = 0.15: $Li_{6.4}Al_{0.05}Ga_{0.15}La_3Zr_2O_{12}$.

The proposed dual substitution of $Li_7La_3Zr_2O_{12}$, in which 0.15 mol Ga^{3+} occupies the Li_{24d} sites while 0.10 mol Sc^{3+} occupies the Zr sites leading to $Li_{6.65}Ga_{0.15}La_3Zr_{1.90}Sc_{0.10}O_{12}$, offers new opportunities for fine-tuning the charge carrier concentration as well as the Li local structure in garnet electrolytes. The accurate control of the crystal chemistry achieved in these materials is possibly the key to enhancing the ionic conductivity, which is of great importance for enabling their practical application in solid state batteries. This strategy could be extrapolated to other inorganic conductors, contributing to the progress toward the design of superionic electrolytes with optimal transport properties.

CONCLUSION

A dual substitution strategy, $Li_{6.55+y}Ga_{0.15}La_3Zr_{2-y}Sc_yO_{12}$, is proposed to investigate the ionic conductivity of cubic garnets with n_{Li} > 6.55, the Ga substitution aimed at stabilizing the cubic crystal structure and the incorporation of Sc at increasing the number of charge carriers. The dual substitution scheme results in a complex cationic distribution with a unique Li local structure. DFT calculations predict a clear preference for Ga occupation of the tetrahedral Li_{24d} sites, which is experimentally confirmed by ^{71}Ga NMR for low Sc substitution level (y = 0.10). The presence of Sc increases the disorder of the Li network at the local scale (i.e., broader distribution of chemical environments), which causes an enhancement of the local mobility of part of the Li population. Further Sc substitution leads to Ga occupation of octahedral Li_{96h} sites, which suppresses the ionic conductivity via possible obstruction of the Li percolation network. Therefore, the existence of a Li^+ population with higher local mobility seems to be related to a Li-only occupation of Li_{96h} sites to promote Li^+ long-range diffusion. These conditions are met in the targeted composition $Li_{6.65}Ga_{0.15}La_3Zr_{1.90}Sc_{0.10}O_{12}$, leading to the highest ionic conductivity observed for the garnets so far, with 1.8×10^{-3} S cm^{-1} at 300 K.

DOI: 10.1021/acs.chemmater.6b05369
Chem. Mater. 2017, 29, 1769−1778

The crystal chemistry concepts and the thorough characterization carried out in this study highlight the complex interconnection between substitution scheme, cationic distribution, Li local environments, and transport properties in garnet-structured electrolytes. Analogous dual substitution strategies will be of interest for other Li-ion conductors, as well as Na-ion conductors, allowing access to the new compositions with higher ionic mobility. The possibility of fine-tuning the mobile ion concentration and/or local structure is expected to have a great impact not only on the field of batteries but also on electrochromics and solid oxide fuel cells.

■ ASSOCIATED CONTENT

Supporting Information

The Supporting Information is available free of charge on the ACS Publications website at DOI: 10.1021/acs.chemmater.6b05369.

Rietveld refinements, microstructures, EDS analysis, and fitting of the EIS spectra for LGLZ_Sc10, LGLZ_Sc15, and LGLZ_Sc20, STEM analysis of LGLZ_Sc20 and ^{1}H NMR, ^{27}Al NMR, ^{45}Sc and ^{7}Li spectral deconvolution, and ^{7}Li T_1 relaxation time analysis for LGLZ_Sc 10 and LGLZ_Sc20 (PDF)

■ AUTHOR INFORMATION

Corresponding Authors

*E-mail: lbuannic@cicenergigune.com.
*E-mail: allordes@cicenergigune.com.

ORCID

Lucienne Buannic: 0000-0003-3055-4058
Javier Carrasco: 0000-0003-3117-6933
Frédéric Aguesse: 0000-0002-5675-0711
Anna Llordés: 0000-0003-4169-9156

Notes

The authors declare no competing financial interest.

■ ACKNOWLEDGMENTS

This research was carried out at CIC Energigune (Spain) and was funded by Gobierno Vasco, within the project framework ETORTEK CIC ENERGIGUNE 2015. A.L. and W.Z. also thank IKERBASQUE for financial support. J.C. acknowledges support by The Royal Society through the Newton Alumnus scheme. The authors thank Nuria Gómez for assistance with ICP measurements and Montserrat Casas-Cabanas for XRD. The authors are also grateful for computer resources of the Barcelona Supercomputer Center (BSC), the UKCP consortium (No. EP/F036884/1) with access to Archer, and the Universidad del País Vasco/Euskal Herriko Unibertsitatea with access to the Arina cluster.

■ REFERENCES

(1) Spotnitz, R.; Franklin, J. Abuse behavior of high-power, lithium-ion cells. *J. Power Sources* **2003**, *113*, 81−100.
(2) Hammami, A.; Raymond, N.; Armand, M. Lithium-ion batteries: Runaway risk of forming toxic compounds. *Nature* **2003**, *424*, 635−636.
(3) Lisbona, D.; Snee, T. A review of hazards associated with primary lithium and lithium-ion batteries. *Process Saf. Environ. Prot.* **2011**, *89*, 434−442.
(4) Golubkov, A. W.; Fuchs, D.; Wagner, J.; Wiltsche, H.; Stangl, C.; Fauler, G.; Voitic, G.; Thaler, A.; Hacker, V. Thermal-runaway experiments on consumer Li-ion batteries with metal-oxide and olivin-type cathodes. *RSC Adv.* **2014**, *4*, 3633−3642.
(5) Scrosati, B.; Garche, J. Lithium batteries: Status, prospects and future. *J. Power Sources* **2010**, *195*, 2419−2430.
(6) Thangadurai, V.; Narayanan, S.; Pinzaru, D. Garnet-type solid-state fast Li ion conductors for Li batteries: critical review. *Chem. Soc. Rev.* **2014**, *43*, 4714−4727.
(7) Tatsumisago, M.; Nagao, M.; Hayashi, A. Recent development of sulfide solid electrolytes and interfacial modification for all-solid-state rechargeable lithium batteries. *J. Asian Ceram. Soc.* **2013**, *1*, 17−25.
(8) Cao, C.; Li, Z.-B.; Wang, X.-L.; Zhao, X.-B.; Han, W.-Q. Recent Advances in Inorganic Solid Electrolytes for Lithium Batteries. *Front. Energy Res.* **2014**, *2*, 25.
(9) Zhu, Y.; He, X.; Mo, Y. Origin of Outstanding Stability in the Lithium Solid Electrolyte Materials: Insights from Thermodynamic Analyses Based on First-Principles Calculations. *ACS Appl. Mater. Interfaces* **2015**, *7*, 23685−23693.
(10) Richards, W. D.; Miara, L. J.; Wang, Y.; Kim, J. C.; Ceder, G. Interface Stability in Solid-State Batteries. *Chem. Mater.* **2016**, *28*, 266−273.
(11) Cussen, E. J. Structure and ionic conductivity in lithium garnets. *J. Mater. Chem.* **2010**, *20*, 5167−5173.
(12) Geiger, C. A.; Alekseev, E.; Lazic, B.; Fisch, M.; Armbruster, T.; Langner, R.; Fechtelkord, M.; Kim, N.; Pettke, T.; Weppner, W. Crystal Chemistry and Stability of "$Li_7La_3Zr_2O_{12}$" Garnet: A Fast Lithium-Ion Conductor. *Inorg. Chem.* **2011**, *50*, 1089−1097.
(13) Thompson, T.; Sharafi, A.; Johannes, M. D.; Huq, A.; Allen, J. L.; Wolfenstine, J.; Sakamoto, J. A Tale of Two Sites: On Defining the Carrier Concentration in Garnet-Based Ionic Conductors for Advanced Li Batteries. *Adv. Energy Mater.* **2015**, *5*, 1500096.
(14) Bernuy-Lopez, C.; Manalastas, W.; Lopez del Amo, J. M.; Aguadero, A.; Aguesse, F.; Kilner, J. A. Atmosphere Controlled Processing of Ga-Substituted Garnets for High Li-Ion Conductivity Ceramics. *Chem. Mater.* **2014**, *26*, 3610−3617.
(15) Rettenwander, D.; Redhammer, G.; Preishuber-Pflügl, F.; Cheng, L.; Miara, L.; Wagner, R.; Welzl, A.; Suard, E.; Doeff, M. M.; Wilkening, M.; Fleig, J.; Amthauer, G. Structural and Electrochemical Consequences of Al and Ga Cosubstitution in $Li_7La_3Zr_2O_{12}$ Solid Electrolytes. *Chem. Mater.* **2016**, *28*, 2384−2392.
(16) Jalem, R.; Rushton, M. J. D.; Manalastas, W.; Nakayama, M.; Kasuga, T.; Kilner, J. A.; Grimes, R. W. Effects of Gallium Doping in Garnet-Type $Li_7La_3Zr_2O_{12}$ Solid Electrolytes. *Chem. Mater.* **2015**, *27*, 2821−2831.
(17) Murugan, R.; Ramakumar, S.; Janani, N. High conductive yttrium doped $Li_7La_3Zr_2O_{12}$ cubic lithium garnet. *Electrochem. Commun.* **2011**, *13*, 1373−1375.
(18) Hitz, G. T.; Wachsman, E. D.; Thangadurai, V. Highly Li-Stuffed Garnet-Type $Li_{7+x}La_3Zr_{2-x}Y_xO_{12}$. *J. Electrochem. Soc.* **2013**, *160*, A1248−A1255.
(19) Shannon, R. D.; Prewitt, C. T. Effective ionic radii in oxides and fluorides. *Acta Crystallogr., Sect. B: Struct. Crystallogr. Cryst. Chem.* **1969**, *25*, 925−946.
(20) Miara, L. J.; Richards, W. D.; Wang, Y. E.; Ceder, G. First-Principles Studies on Cation Dopants and Electrolyte|Cathode Interphases for Lithium Garnets. *Chem. Mater.* **2015**, *27*, 4040−4047.
(21) Perdew, J. P.; Ruzsinszky, A.; Csonka, G. I.; Vydrov, O. A.; Scuseria, G. E.; Constantin, L. A.; Zhou, X.; Burke, K. Restoring the Density-Gradient Expansion for Exchange in Solids and Surfaces. *Phys. Rev. Lett.* **2008**, *100*, 136406.
(22) Kresse, G.; Furthmüller, J. Efficient iterative schemes for *ab initio* total-energy calculations using a plane-wave basis set. *Phys. Rev. B: Condens. Matter Mater. Phys.* **1996**, *54*, 11169−11186.
(23) Kresse, G.; Marsman, M.; Furthmüller, J. *Vienna Ab-initio Simulation Package*, Version 5.4.1; Computational Materials Physics, University of Vienna: Vienna. www.vasp.at/.
(24) Kresse, G.; Joubert, D. From ultrasoft pseudopotentials to the projector augmented-wave method. *Phys. Rev. B: Condens. Matter Mater. Phys.* **1999**, *59*, 1758−1775.

DOI: 10.1021/acs.chemmater.6b05369
Chem. Mater. 2017, 29, 1769−1778

(25) Awaka, J.; Takashima, A.; Kataoka, K.; Kijima, N.; Idemoto, Y.; Akimoto, J. Crystal Structure of Fast Lithium-ion-conducting Cubic $Li_7La_3Zr_2O_{12}$. *Chem. Lett.* **2011**, *40*, 60−62.
(26) Ewald, P. P. Die Berechnung optischer und elektrostatischer Gitterpotentiale. *Ann. Phys.* **1921**, *369*, 253−287.
(27) Lander, L.; Reynaud, M.; Carrasco, J.; Katcho, N. A.; Bellin, C.; Polian, A.; Baptiste, B.; Rousse, G.; Tarascon, J.-M. Unveiling the electrochemical mechanisms of $Li_2Fe(SO_4)_2$ polymorphs by neutron diffraction and density functional theory calculations. *Phys. Chem. Chem. Phys.* **2016**, *18*, 14509−14519.
(28) Rodríguez-Carvajal, J. Recent advances in magnetic structure determination by neutron powder diffraction. *Phys. B* **1993**, *192*, 55−69.
(29) Massiot, D.; Fayon, F.; Capron, M.; King, I.; Le Calvé, S.; Alonso, B.; Durand, J.-O.; Bujoli, B.; Gan, Z.; Hoatson, G. Modelling one- and two-dimensional solid-state NMR spectra. *Magn. Reson. Chem.* **2002**, *40*, 70−76.
(30) Wang, Y.; Yan, P.; Xiao, J.; Lu, X.; Zhang, J.-G.; Sprenkle, V. L. Effect of Al_2O_3 on the sintering of garnet-type $Li_{6.5}La_3Zr_{1.5}Ta_{0.5}O_{12}$. *Solid State Ionics* **2016**, *294*, 108−115.
(31) Rangasamy, E.; Wolfenstine, J.; Sakamoto, J. The role of Al and Li concentration on the formation of cubic garnet solid electrolyte of nominal composition $Li_7La_3Zr_2O_{12}$. *Solid State Ionics* **2012**, *206*, 28−32.
(32) Rettenwander, D.; Geiger, C. A.; Tribus, M.; Tropper, P.; Amthauer, G. A Synthesis and Crystal Chemical Study of the Fast Ion Conductor $Li_{7-3x}Ga_xLa_3Zr_2O_{12}$ with x = 0.08 to 0.84. *Inorg. Chem.* **2014**, *53*, 6264−6269.
(33) Rettenwander, D.; Langer, J.; Schmidt, W.; Arrer, C.; Harris, K. J.; Terskikh, V.; Goward, G. R.; Wilkening, M.; Amthauer, G. Site Occupation of Ga and Al in Stabilized Cubic $Li_{7-3(x+y)}Ga_xAl_yLa_3Zr_2O_{12}$ Garnets As Deduced from ^{27}Al and ^{71}Ga MAS NMR at Ultrahigh Magnetic Fields. *Chem. Mater.* **2015**, *27*, 3135−3142.
(34) Kim, N.; Hsieh, C.-H.; Stebbins, J. F. Scandium Coordination in Solid Oxides and Stabilized Zirconia: ^{45}Sc NMR. *Chem. Mater.* **2006**, *18*, 3855−3859.
(35) Buannic, L.; Blanc, F.; Hung, I.; Gan, Z.; Grey, C. P. Probing the local structures and protonic conduction pathways in scandium substituted $BaZrO_3$ by multinuclear solid-state NMR spectroscopy. *J. Mater. Chem.* **2010**, *20*, 6322−6332.
(36) Oikawa, I.; Takamura, H. ^{45}Sc NMR spectroscopy and first-principles calculation on the symmetry of ScO_6 polyhedra in BaO-Sc_2O_3-based oxides. *Dalton Trans.* **2014**, *43*, 9714−9721.
(37) Buschmann, H.; Dolle, J.; Berendts, S.; Kuhn, A.; Bottke, P.; Wilkening, M.; Heitjans, P.; Senyshyn, A.; Ehrenberg, H.; Lotnyk, A.; Duppel, V.; Kienle, L.; Janek, J. Structure and dynamics of the fast lithium ion conductor "$Li_7La_3Zr_2O_{12}$". *Phys. Chem. Chem. Phys.* **2011**, *13*, 19378−19392.
(38) Düvel, A.; Kuhn, A.; Robben, L.; Wilkening, M.; Heitjans, P. Mechanosynthesis of Solid Electrolytes: Preparation, Characterization, and Li Ion Transport Properties of Garnet-Type Al-Doped $Li_7La_3Zr_2O_{12}$ Crystallizing with Cubic Symmetry. *J. Phys. Chem. C* **2012**, *116*, 15192−15202.
(39) Hubaud, A. A.; Schroeder, D. J.; Key, B.; Ingram, B. J.; Dogan, F.; Vaughey, J. T. Low temperature stabilization of cubic $(Li_{7-x}Al_{x/3})$-$La_3Zr_2O_{12}$: role of aluminum during formation. *J. Mater. Chem. A* **2013**, *1*, 8813−8818.
(40) Rettenwander, D.; Blaha, P.; Laskowski, R.; Schwarz, K.; Bottke, P.; Wilkening, M.; Geiger, C. A.; Amthauer, G. DFT Study of the Role of Al^{3+} in the Fast Ion-Conductor $Li_{7-3x}Al^{3+}{}_xLa_3Zr_2O_{12}$ Garnet. *Chem. Mater.* **2014**, *26*, 2617−2623.
(41) Müller, D.; Gessner, W.; Behrens, H. J.; Scheler, G. Determination of the aluminium coordination in aluminium-oxygen compounds by solid-state high-resolution ^{27}Al NMR. *Chem. Phys. Lett.* **1981**, *79*, 59−62.
(42) Sarou-Kanian, V.; Gleizes, A. N.; Florian, P.; Samélor, D.; Massiot, D.; Vahlas, C. Temperature-Dependent 4-, 5- and 6-Fold Coordination of Aluminum in MOCVD-Grown Amorphous Alumina Films: A Very High Field ^{27}Al-NMR study. *J. Phys. Chem. C* **2013**, *117*, 21965−21971.
(43) MacKenzie, K. J. D.; Smith, M. E. *Multinuclear Solid-State Nuclear Magnetic Resonance of Inorganic Materials*; Pergamon: Amsterdam, 2002.
(44) Kuhn, A.; Kunze, M.; Sreeraj, P.; Wiemhöfer, H. D.; Thangadurai, V.; Wilkening, M.; Heitjans, P. NMR relaxometry as a versatile tool to study Li ion dynamics in potential battery materials. *Solid State Nucl. Magn. Reson.* **2012**, *42*, 2−8.
(45) Matsui, M.; Takahashi, K.; Sakamoto, K.; Hirano, A.; Takeda, Y.; Yamamoto, O.; Imanishi, N. Phase stability of a garnet-type lithium ion conductor $Li_7La_3Zr_2O_{12}$. *Dalton Trans.* **2014**, *43*, 1019−1024.
(46) Nemori, H.; Matsuda, Y.; Matsui, M.; Yamamoto, O.; Takeda, Y.; Imanishi, N. Relationship between lithium content and ionic conductivity in the $Li_{5+2x}La_3Nb_{2-x}Sc_xO_{12}$ system. *Solid State Ionics* **2014**, *266*, 9−12.
(47) Hellstrom, E. E.; Van Gool, W. Li ion conduction in Li_2ZrO_3, Li_4ZrO_4, and $LiScO_2$. *Solid State Ionics* **1981**, *2*, 59−64.

DOI: 10.1021/acs.chemmater.6b05369
Chem. Mater. 2017, 29, 1769−1778